





Experimental studies on the frequency selection in flat plate wakes: Mean-flow stability analyses and low-dimensional modeling

Dipankar Dutta ¹, Indra Kanshana ¹, Shyam Sunder Gopalakrishnan ^{2,3,*}
and A. C. Mandal ^{1,†}

¹*Department of Aerospace Engineering, Indian Institute of Technology, Kanpur 208016, India*

²*Faculté des Sciences, Université libre de Bruxelles (ULB), 1050 Brussels, Belgium*

³*Laboratoire de Physique des Lasers, Atomes et Molécules,
CNRS UMR 8523, 59655 Villeneuve d'Ascq Cedex, France*



(Received 31 May 2021; accepted 4 March 2022; published 14 April 2022)

We investigate the global frequency selection of two-dimensional vortex shedding in the flat plate wake. The analysis is based on the mean-flow velocity profiles obtained from experimental measurements carried out for two values of Reynolds number, 1850 and 3350, which are based on the plate thickness and the free-stream velocity. Two different trailing edge geometries of the flat plate are considered in this study: blunt and circular. By performing local spatiotemporal analyses on the measured mean-flow velocity profiles, we estimate the global shedding frequency of the flow. This is in excellent agreement with the shedding frequency measured experimentally. To complement the study, we carry out a low-dimensional modeling based on the proper orthogonal decomposition (POD) of the flow fields which is novel for flat plate wakes. We observe that a model based on only two POD modes produces an accurate estimate of the global shedding frequency. Our results also highlight the role of the interaction strength between the mean flow and the higher harmonics thereby experimentally supporting the theoretical criterion outlined in Sipp and Lebedev [*J. Fluid Mech.* **593**, 333 (2007)].

DOI: [10.1103/PhysRevFluids.7.044102](https://doi.org/10.1103/PhysRevFluids.7.044102)

I. INTRODUCTION

Since the seminal work by Strouhal [1] the frequency selection of periodic vortex shedding in the wakes of flows past obstacles has been of interest to both researchers and engineers [2–6]. With the advances in experimental measurements, the frequency selection criterion has been proposed [6–8] and has been successfully built in the framework of weakly nonparallel flows [5,7,9–12]. Interestingly, the selection criterion when applied to the mean flow of bluff-body wakes has shown to yield particularly good results for the prediction of the frequency of the unsteadiness. This has been observed in the wake formed by a rectangular forebody [13], and by a cylinder [12], and has been confirmed by performing a global stability analysis on the mean flow of a cylinder wake [14,15]. The theoretical support for these observations was advanced by Sipp and Lebedev [16] where they outlined the conditions when the stability of a mean flow would approximately match with the nonlinear frequency of the unsteady wake. Using a weakly global nonlinear analysis in the vicinity of the critical Reynolds number, they showed that the frequency selection is governed by the relative interaction strength of the mean flow and the higher harmonics. Specifically, the global frequency is well predicted by a mean-flow analysis when the nonlinear interaction of the

*shyam7sunder@gmail.com

†alakeshm@iitk.ac.in

zeroth (mean-flow) harmonic with the first harmonic is significantly higher than the interaction of the second harmonic with the first harmonic. They observed that the linear stability analysis of the mean flow yields good results for a cylinder wake, but does not provide a meaningful insight in the case of an open cavity flow. In addition, it has been noted in Refs. [12,17,18] that the global frequency is well estimated by the local absolute frequency at the stagnation point in the flow. In this study, we address these concerns for flat plate wakes using experimentally measured mean-flow velocity profiles, a case that is missing in the literature.

The wake formed by the trailing edge of a flat plate, or a thin aerofoil at zero incidence, has been extensively studied in the past in the laminar, transitional, and turbulent regimes [19–28]. Understanding the frequency selection in flat plate wakes is of particular importance as they find direct applications in the aerospace industry, where drag reduction and noise control are desired [24,29], in the design of turbine and compressor blades [30]. From an academic point of view, flat plate remains one of the simplest geometrical configurations which result in complex wake characteristics which resemble turbulent wakes behind industrial objects such as bridges, cooling towers, and gas turbine blades [30]. In addition, the frequency selection in flat plate wakes is of interest to further the understanding of laminar to turbulence transition in such scenarios. The flat plate wake is influenced by the profile of the trailing edge. Carefully made measurements by Nishioka and Miyagi [21] have shown that the wake behind a flat plate with a sharp trailing edge can be kept laminar even at a Reynolds number of 3000 (based on the freestream velocity and the plate length), even though a wake flow is inherently unstable. The turbulent wake characteristics of flat plates with a sharp trailing edge have been well investigated [22,24,25]. In contrast, there exists vigorous vortex shedding for flat plates with a blunt trailing edge [31,32]. The vortex shedding from flat plates with square leading and trailing edges were experimentally studied in Ref. [31] where they showed that the separated shear layer becomes unstable downstream of the trailing edge corner. As maintaining extremely sharp trailing edges for flat plates still pose as engineering challenges, it is pertinent to study the effect of the trailing edge geometry, and is thus considered in the present study. In addition to the trailing edge geometry [30,32,33], the characteristics of the flat plate wake depends on the velocities in the upper and lower surfaces of the plate [34], and various other boundary layer parameters such as the boundary layer thickness and shape factor [30,35,36].

One of the first experimental measurements on the vortex shedding behind thin flat plates were made by [3]. The hydrodynamic resonance criteria advanced by Koch [37] based on a local stability analysis predicts well the observed shedding frequency in Ref. [3], which is governed by the streamwise location where the instability character changes from an absolute to a convective nature. Apart from the global frequency selection criterion proposed in Ref [37], there are other criteria such as the maximum growth criterion by Pierrehumbert [38], and the initial growth criterion by Monkewitz and Nguyen [39]. In a strictly linear setting, the first rigorous selection criterion has been established in Ref. [7], with the global frequency given by a saddle-point condition based on an analytic continuation of absolute instability frequency in the complex $x = (x_r, x_i)$ plane. This criterion is seen to accurately predict the selected frequency in the wake of a blunt-edged plate [13] using the time-mean flow. Since then the nonlinear instability of slowly divergent flows has been addressed in Refs. [11,12] with the bifurcation to self-sustained oscillation in two-dimensional wake flows being triggered whenever a region of local absolute instability exists in the flow. The dominant shedding frequency is imposed by the first absolutely unstable downstream station. As observed in Ref. [13], it has been shown in Ref. [12] that the time average of the oscillating wake behind a cylinder provided the best profile to predict the vortex shedding frequency.

It is to be noted that the cylinder wake studied in Ref. [12] goes from being locally convective to absolutely unstable within a finite region, with the frequency at this transition station fixing the global shedding frequency, arising from a balance between upstream perturbation growth and downstream advection [12,40]. However, the wake of the blunt-edged plate studied in Ref. [13] is locally absolutely unstable at the blunt trailing edge. The first absolutely unstable downstream station in this case would correspond to the streamwise location proposed in Ref. [37]. This observation is detailed in the criterion proposed in Ref. [39] where the initial growth of the

disturbances within the convectively unstable region downstream of the bluff-body, the extent of which then subsequently fixes the spatial scale associated with the global shedding frequency. As mentioned earlier, using a weakly global analysis Sipp and Lebedev [16] theoretically outlined the conditions when the frequency obtained from a linear stability analysis based on the mean flow matches with the global shedding frequency of the wake. This is governed by the interaction strength of the higher harmonics with the mean-flow harmonic. Using a local stability analysis based on experimentally measured velocity profiles Khor *et al.* [41] showed that the time-averaged mean flows yield an accurate estimate of the global shedding frequency for the wake of a cylinder. However, such an experimental study is missing in the literature for flat plate wakes. We investigate the above-discussed characteristics for the wake of a flat plate with a blunt/circular trailing edge by performing a local stability analysis using the time-averaged flows, and compare them with the global shedding frequency. By quantifying the interaction strengths between the mean-flow and higher harmonics, we also support the theoretical criterion reported by Sipp and Lebedev [16] using experimentally obtained flow fields which is novel in the literature.

The characteristics of the wake formed by a circular cylinder, and by a flat plate with a circular trailing edge are indeed different. This aspect is studied in Ref. [42] where they carried out a Floquet stability analysis to investigate the transition scenario in the wake behind a flat plate with a circular trailing edge, referred to as an elongated cylinder with an aerodynamic leading edge, and with a blunt trailing edge. The aspect ratio (chord length to thickness) of a compact body fixes the boundary layer characteristics at the trailing edge, the role of which was investigated in Ref. [42]. Their study revealed the existence of three different modes, showing similarities and differences between the two different wakes, concluding that the transition scenario in the wake of a flat plate with a circular trailing edge may not be completely generic, as often assumed based on cylinder wakes. In addition, they showed that the transition Reynolds number did not vary linearly with respect to the aspect ratio, thereby concluding that the transition Reynolds number does not require that the boundary layer thickness should be similar at the trailing edge as the flow enters the wake. The observations made in Ref. [42] have been experimentally confirmed in Refs. [43–45] wherein they indicate that the wake topology and their instability at the trailing edge of a flat plate are different from those observed in the case of a compact body. Furthermore the wake characteristics of a flat plate with circular and elliptic trailing edges were numerically studied in Ref. [32], where they concluded that the streamlining of a trailing edge results in weaker vortex shedding, with a smaller separated region.

Similarly, various studies have revealed the differences in the secondary instability mechanisms and the resulting vortical structures downstream of a flat plate [26,46] from that of a cylinder wake [14,47]. The flat plate wake flows were experimentally studied at low Reynolds numbers in Ref. [26] which were formed by the merging of two parallel laminar streams at the trailing edge. It is observed that the leading modes are characterized by the same wavelength unlike in a cylinder wake, indicating that they arise from the same mechanism, which is a combination of hyperbolic and elliptical instability. These observations have been corroborated numerically in Ref. [46]. The differences in bluff body wakes from that of a flat plate stem from the fact that the shear layers in bluff-body wakes separate at a certain location on the surface of the body, thus introducing a second characteristic length in the problem, whereas in a flat plate wake, the flow separation occurs right at the trailing edge. In addition, the base flow varies rapidly behind a cylinder and is characterised by flow reversal with highly concentrated vorticity regions. In this region, the secondary instability is absolutely unstable due to a global secondary bifurcation [48], whereas for a flat plate the instability is convective [26].

In this work, we investigate the global frequency of flat plate wakes by performing a local stability analysis on the mean-flow fields. A blunt (square/rectangular) and a circular profile for the trailing edge geometry are considered in this study which are shown in Figs. 1(a) and 1(b). The experiments were conducted in a wind tunnel, a schematic sketch of which is shown in Fig. 1(c). The two-dimensional velocity fields were obtained by using a time-resolved particle image velocimetry (TR-PIV) technique. The study is carried out for two values of the Reynolds number, 1850 and

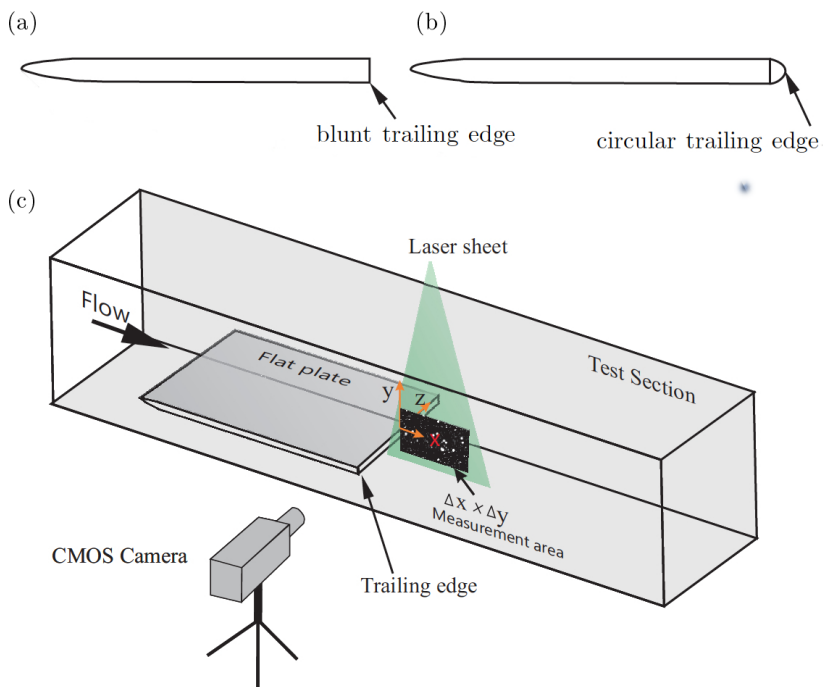


FIG. 1. The experimental setup used in the present study on flat plate wakes. Two profiles of the flat plate are considered, with completely blunt (a) and circular (b) trailing edges, respectively. (c) Illustration of the TR-PIV measurement setup.

3350, based on the freestream velocity and the plate thickness. Using the obtained flow fields, we perform a local spatiotemporal stability analysis on the mean velocity profiles at different streamwise locations of the unsteady wake. The selected global frequency is then compared with the different characteristic frequencies discussed earlier. It has been observed that the local absolute frequency at the end of the absolutely unstable domain of the flow predicts the global shedding frequency. As observed in other bluff-body flows, the global frequency of the wake is well predicted by the local absolute frequency at the stagnation point in the flow. An excellent pedagogical review on the theoretical tools used in the present study can be found in Ref. [49].

To complement the study, we analyze the experimental data by carrying out a proper orthogonal decomposition (POD) of the wake velocity fields. POD is a useful tool, especially in experimental investigations, which is capable of extracting information using snapshots of the flow fields [50–57]. It provides a set of orthogonal and optimal basis functions, onto which the Navier–Stokes equations can be projected to construct a reduced order model [58,59]. We perform the POD analysis on the fluctuations of the wake velocity fields by removing the mean flow. It is observed that over 80% of the energy of the unsteady wake is captured by the first 10 POD modes and over 70% of the energy by the first two POD modes, even for the higher Reynolds number considered here, indicating the flow under consideration has low inherent dimensionality. Therefore, a low-dimensional model based on the dominant POD modes is found to yield an accurate estimate of the selected global frequency. Similar observations have been reported for a cylinder wake using POD analyses [54]. In doing so, we experimentally support the theoretical criterion outlined in Ref. [16] which determines whether a mean-flow stability analysis is meaningful and can predict the global shedding frequency, based on the interaction strength of the mean flow with its higher harmonics.

To this end, we organize the paper as follows. The flow configuration, along with the theoretical, experimental, and numerical tools used in the current study are briefly outlined in Sec. II. Following

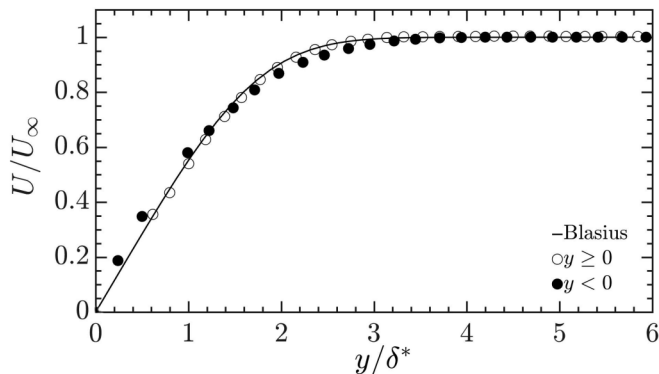


FIG. 2. Boundary layer profile at $0.45D$ (i.e., at $x = -0.45D$) from the blunt trailing edge of the flat plate for $Re = 3350$. Open and filled circles denote the velocity profiles above and below the flat plate, respectively. Here, δ^* denotes the displacement thickness. The Blasius solution is shown using the solid black line.

this, in Sec. III we present the mean-flow velocity profiles using which the spatiotemporal stability analyses are performed. The results from POD analysis with a description of the flow features of a flat plate wake are presented in Sec. IV. The paper finishes with a discussion on the global shedding frequency of flat plate wakes along with some concluding remarks in Sec. V.

II. FLOW CONFIGURATION AND METHODOLOGY

A. Experimental setup

The general flow configuration consists of an incompressible fluid stream over a flat plate with a blunt/circular trailing edge, a schematic of which is shown in Fig. 1. Shape of the leading edge of the plate is a super ellipse, details of which are available in Ref. [60]. A wake forms downstream of the flat plate from the fixed separation points at the trailing edge. Whole field measurements in the wake of the flat plate were carried out using the TR-PIV technique in a low-speed wind tunnel. The wind tunnel used in the present study is an open circuit suction type wind tunnel. The settling chamber of this tunnel houses a honeycomb and six turbulence reduction screens. However, the settling chamber is followed by a contraction cone of 16 : 1. The 3000-mm-long test section of the tunnel has a square cross section of 610 mm \times 610 mm, and is followed by a diffuser. The three bladed fan of this tunnel is powered by a 14.5-kW alternating current motor. The tunnel turbulent intensity measured in the test section is found to be 0.1% of the freestream velocity (for details, see Ref. [60]). The flat plate has a thickness of 12 mm and a length of 700 mm and is mounted horizontally in the midplane of the test section of the tunnel. In the following x , y , and z represent streamwise, wall normal, and spanwise directions, respectively. The free stream velocity U_∞ and the flat plate thickness D were used as the velocity and length scales, with the Reynolds number given by $Re = U_\infty D/\nu$. In the present study two values of Re are considered: 1850 and 3350, which are carefully chosen so that the boundary layer remains laminar till it reaches the trailing edge of the flat plate. The boundary layer profile at a distance of $0.45D$ from the blunt trailing edge at $Re = 3350$ is shown in Fig. 2. The velocity profile closely matches with the Blasius solution, thereby ensuring that the boundary layer remains laminar for both values of Re chosen in this investigation.

The TR-PIV measurements were carried out at the trailing edge of the flat plate, as schematically shown in Fig. 1. The TR-PIV system consists mainly of a 4-megapixel CMOS camera with 365-Hz repetition rate in double exposure mode at full resolution (IDT vision, USA), a Nd-YLF dual head PIV laser with 30-mJ/pulse at 1-kHz repetition rate (Photonics Industries International Inc, USA), and an IDT synchronizer. Using the inboard memory of the CMOS camera, 365 TR-PIV image pairs were captured per second at full resolution. The flow was seeded using a fog generator. Using

appropriate sheet forming optics, a thin laser sheet of about 1-mm thickness was produced at the region of interest, as shown in Fig. 1. Using the ProVISION XS package procured from IDT, the images of the seeding particles in the streamwise wall-normal (x - y) plane were then acquired over a region of interest $\approx 66 \text{ mm} \times 60 \text{ mm}$. The acquired images were then processed in ProVISION XS using a correlation window of 32 pixels \times 32 pixels. Mean quantities were estimated based on 800 PIV realizations, which were spread over several shedding cycles. The ProVISION XS is based on mesh free algorithm as detailed in Ref. [61]. This software package and the PIV system were also used in our various previous works (e.g., Refs. [60,62–64]). Following [60] an uncertainty analysis for the measured velocity fields has been carried out, and the maximum uncertainty is found to be around 2% of the freestream velocity. The resulting uncertainty in circular frequency is found to be 2.7%.

B. Local stability analysis

The global shedding frequency of bluff-body wakes can be determined from a local stability analysis based on the concept of absolute instability [7,9,10,65]. There exists a precise location in the complex x plane which acts as a wavemaker for the entire field, thereby fixing the global frequency. Following Refs. [11,12,18], we boldly ignore the highly nonparallel nature of the flat plate wake, even though the Reynolds numbers are on the higher side of the laminar range. This is due to the fact that the most unstable modes are two-dimensional which follows the Squire's theorem [66]. We derive the local characteristics at a streamwise location by freezing the x coordinate, and by performing a linear stability on the measured mean-flow velocity profiles, $U(y) = U_b(x, y)$. Linearizing around this basic flow by adding a small amplitude perturbation (u'_x, u'_y), gives us the linearized Navier-Stokes equations

$$\begin{aligned} \partial_t u'_x + U \partial_x u'_x + u'_y \partial_y U &= -\partial_x p' + \text{Re}^{-1} \nabla^2 u'_x, & \partial_t u'_y + U \partial_x u'_y &= -\partial_y p' + \text{Re}^{-1} \nabla^2 u'_y, \\ \partial_x u'_x + \partial_y u'_y &= 0. \end{aligned} \quad (1)$$

We look for traveling wave solutions in the form of normal modes as $q'(x, y, t) = q(y) \exp[i(kx - \omega t)]$ where $\omega (= \omega_r + i\omega_i)$ is the complex frequency, and $k (= k_r + ik_i)$ is the complex wave number; $q'(x, y, t) = [u'_x, u'_y, p']^T$. The linear stability of these waves are governed by the Orr-Sommerfeld equation [67]:

$$\left[(-i\omega + ikU) \left(\frac{d^2}{dy^2} - k^2 \right) - ik \frac{d^2 U}{dy^2} - \frac{1}{\text{Re}} \left(\frac{d^2}{dy^2} - k^2 \right)^2 \right] u_y = 0, \quad (2)$$

where the wave number k is nondimensionalized by the flat plate thickness D , and ω by D and the freestream velocity U_∞ . The Orr-Sommerfeld equation (2) along with the boundary conditions $u_y = \frac{du_y}{dy} = 0$ (in the free stream) is then solved using standard spectral methods [68] which yields the local dispersion relation $\omega = \Omega^l(k, x)$. For doing this, the measured mean-flow velocity profile at a streamwise location is spatially discretized on $N_y = 100$ Chebyshev collocation points in the wall normal direction ($x_j = \cos(\frac{j\pi}{N_y}) \in [-1, 1]$, $j = 0, 1, \dots, N_y$). By applying the classical Briggs-Bers criterion [12,69,70] of zero group velocity condition the absolute frequency $\omega_0(x)$ is then obtained. As part of the current study, the spatiotemporal analysis of a parallel model wake flow at a low Reynolds number is carried out. Following Refs. [9,17], the profile of the basic flow is given by

$$U(y) = 1 - R + 2RF(y), \quad (3)$$

$$R = \frac{U_c^* - U_\infty^*}{U_c^* + U_\infty^*}, \quad (4)$$

$$F(y) = \{1 + \sinh^{2N}[y \sinh^{-1}(1)]\}^{-1}, \quad (5)$$

where N is the shape parameter. The superscript $*$ denotes a dimensional quantity, with U_c being the centerline velocity ($y = 0$), and U_∞ the freestream velocity. Figure 3(a) shows the parallel model

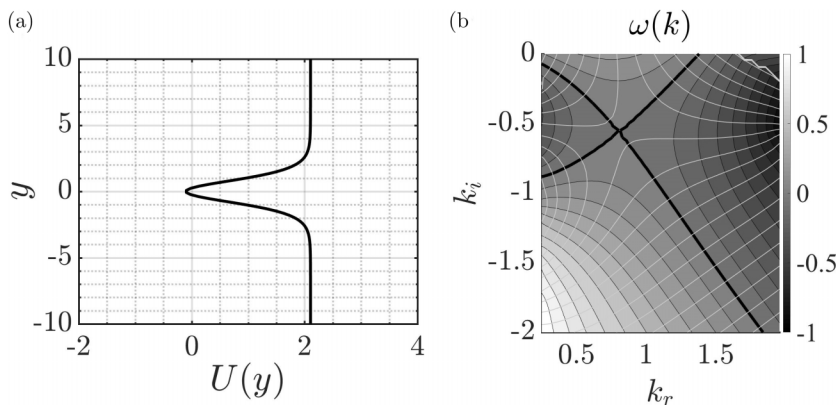


FIG. 3. (a) Parallel model wake velocity profile $U(y)$ and (b) the contours of ω_i (grayscale) and ω_r (graylines) at $\text{Re} = 11.3$, $R = -1$, $N = 2$. The thick black line is $\omega_i = 0$. The normalization has been carried out as in Ref. [9].

wake profile at a Reynolds number 11.3 (based on the average basic flow velocity and the wake half-width), $R = -1$, and $N = 2$. The variation of ω_r and ω_i in the complex k plane is shown in Fig. 3(b). The absolute wave number $k_0 = 0.8047 - 0.5569i$, and the absolute frequency $\omega_0 = 1.0086 + 0i$ is in excellent agreement with Ref. [9].

C. POD analysis and low-dimensional modeling

1. POD methodology

The POD analysis of the unsteady flat plate wake is based on the commonly used “method of snapshots” proposed in Ref. [71], to find the dominant POD modes/eigenfunctions. The discrete data of the fluctuations of the velocity field are obtained from PIV measurements, and are arranged in vectors [62,72] as

$$\Psi_i = \mathbf{V}_i - \frac{1}{M} \sum_{j=1}^M \mathbf{V}_j, \quad i = 1, 2, \dots, M, \quad (6)$$

where M is the number of ensemble and \mathbf{V}_j is the instantaneous velocity field corresponding to the j th PIV realization. From these velocity fluctuations, as the mean-flow fields are removed, the elements of a covariance matrix are formed as

$$R_{ij} = (\Psi_i, \Psi_j). \quad (7)$$

The covariance matrix R is a $M \times M$ symmetric matrix with non-negative eigenvalues, λ . These eigenvalues correspond to the energy of the respective POD mode. The energy fraction of the k th mode is given by $E_k = \lambda_k/E$, where E is the total energy of the POD modes.

The eigenfunctions, Φ^k , are constructed using the eigenvectors of the covariance matrix as,

$$\Phi^k = \sum_{i=1}^M \phi_i^k \Psi_i, \quad k = 1, \dots, M, \quad (8)$$

where ϕ_i^k is the i th component component of the k th eigenvector, and the eigenfunctions are normalized such that $(\Phi^k, \Phi^l) = \delta_{kl}$, where δ_{kl} denotes the Kronecker delta [62]. Using the eigenfunction system Φ^k , one can expand the fluctuating velocity field, $\mathbf{v}(\mathbf{x}, t)$ as

$$\mathbf{v}(\mathbf{x}, t_n) = \sum_k a^k(t_n) \Phi^k(\mathbf{x}), \quad (9)$$

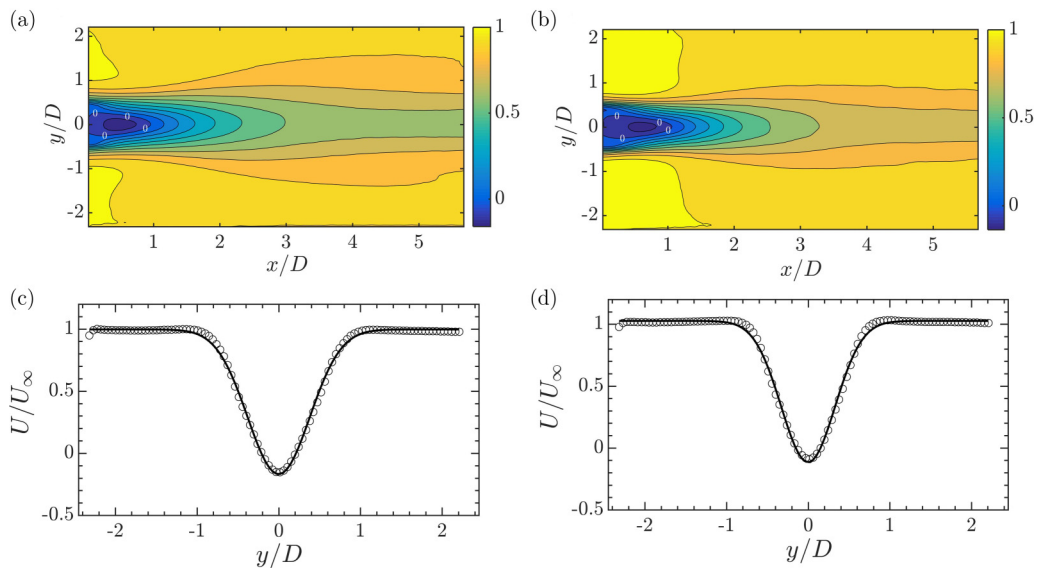


FIG. 4. Mean-flow fields of the wake of a flat plate with a blunt trailing edge. The spatial distribution of the time-averaged mean-flow fields of streamwise velocity component for (a) $Re = 1850$ and (b) $Re = 3350$. The zero contour represents the extent of the recirculation zone. The wall-normal mean velocity profile $U(y) = U_b(x, y)$ at (c) $x/D = 0.86$ for $Re = 1850$ and (d) $x/D = 0.56$ for $Re = 3350$. The continuous lines represent the best fit mean-flow velocity profiles given by Eq. (17) which are used in the local spatiotemporal stability analyses, with (c) $c_1 = -1.165$, $c_2 = 0.289$, and $c_3 = 0.996$, and (d) $c_1 = -1.141$, $c_2 = 0.217$, and $c_3 = 1.026$.

where the time coefficients, $a^k(t_n)$, are obtained by projecting the instantaneous snapshots on the eigenfunctions, i.e.,

$$a^k(t_n) = (\mathbf{v}(\mathbf{x}, t_n), \Phi^k(\mathbf{x})), \quad (10)$$

where (\cdot) represents an inner product in the function space.

2. Low-dimensional modeling

Galerkin projection is a suitable method to get an evolution equation of the time/expansion coefficients, $a(t)$, and the POD eigenfunctions provide a suitable basis for Galerkin projection (see Ref. [73], for details). Therefore, one can project the Navier-Stokes equations on the POD eigenfunctions to get a low-dimensional model consisting of a system of ordinary differential equations for the time coefficients. For Galerkin projection, we follow the formulation presented in Refs. [57,59]. Since POD eigenfunctions satisfy the continuity equation, we consider the following momentum equation for the instantaneous velocity, \mathbf{V} . Neglecting the body force term and considering incompressible flow, the momentum equation for the instantaneous velocity, \mathbf{V} , reads as

$$\frac{\partial \mathbf{V}}{\partial t} + \mathbf{V} \cdot \nabla \mathbf{V} = -\frac{\nabla P}{\rho} + \nu \Delta \mathbf{V}, \quad (11)$$

where P is the pressure and ν is the kinematic viscosity. Substituting $\mathbf{V} = \bar{\mathbf{V}} + \mathbf{v}$ in Eq. (11), where $\bar{\mathbf{V}}$ and \mathbf{v} are the mean and the fluctuating parts of the velocity, and subtracting the time-averaged momentum equation, we obtain

$$\frac{\partial \mathbf{v}}{\partial t} + \mathbf{v} \cdot \nabla \bar{\mathbf{V}} + \bar{\mathbf{V}} \cdot \nabla \mathbf{v} + \mathbf{v} \cdot \nabla \mathbf{v} - \overline{\mathbf{v} \cdot \nabla \mathbf{v}} = -\frac{1}{\rho} \nabla p + \nu \Delta \mathbf{v}, \quad (12)$$

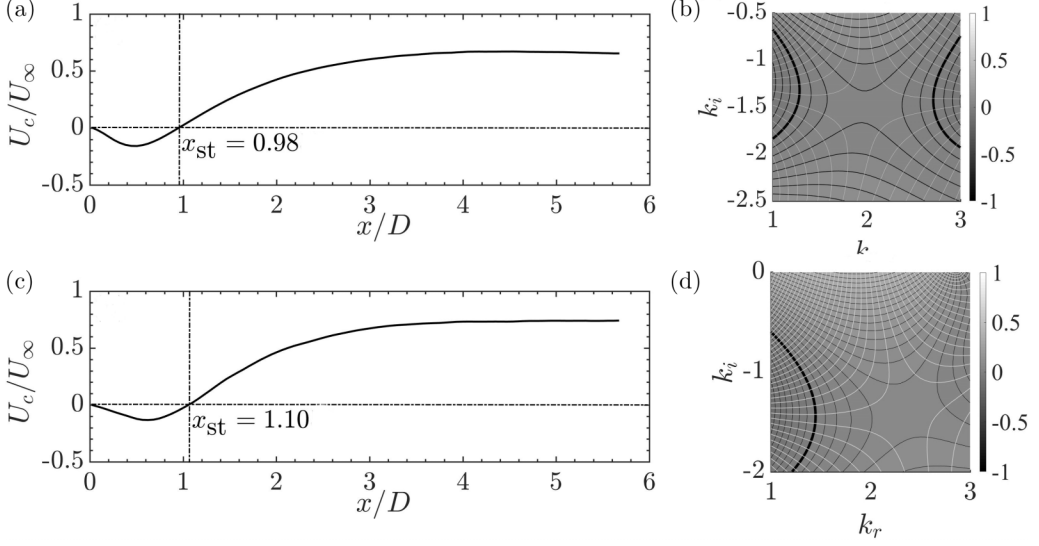


FIG. 5. Variation of the centerline velocity as a function of the downstream distance behind the blunt trailing edge of the flat plate. Parameter settings: (a) $Re = 1850$ and (c) $Re = 3350$. (b, d) Contours of ω_i (grayscale) and ω_r (graylines) at $Re = 1850$ and $Re = 3350$ at the corresponding stagnation points. The thick black line denotes $\omega_i = 0$.

where p is the fluctuating pressure. Using the Eq. (9) in the above, and projecting the resulting equation on the POD modes, Φ_k , we have

$$\frac{da^k}{dt} = A^{ki} a^i + B^{kil} (a^i a^l - \overline{a^i a^l}) + C^k, \quad (13)$$

where the coefficients are given by

$$A^{ki} = -(\Phi^k, \Phi^i \cdot \nabla \bar{\mathbf{V}}) - (\Phi^k, \bar{\mathbf{V}} \cdot \nabla \Phi^i) + \nu(\Phi^k, \Delta \Phi^i), \quad (14)$$

$$B^{kil} = -(\Phi^k, \Phi^i \cdot \nabla \Phi^l), \quad (15)$$

$$C^k = -\frac{1}{\rho}(\Phi_k, \nabla p). \quad (16)$$

Note that $\overline{a^k a^l} = \delta_{kl} \lambda_k$ as the coefficients are uncorrelated. Utilizing the given POD modes and the mean velocities, one can calculate the coefficients of Eq. (13). Further, one can find that $C^k = 0$, considering homogenous boundary conditions and divergence free nature of the POD modes (see Ref. [59] for further details).

III. MEAN-FLOW FIELDS AND SHEDDING FREQUENCY

We now present the mean velocity fields of the flat plate wake obtained for blunt, and circular, trailing edges for two values of the Reynolds number. Figure 4 shows the time-averaged velocity profiles of the flat plate wake with a blunt trailing edge. The spatial distribution of the mean-flow fields, $U_b(x, y)$, are presented in Figs. 4(a) and 4(b). Directly downstream of the trailing edge, the flow reverses, as can be seen from the negative values of the centerline velocity. Moving downstream along the flat plate wake, we can observe that the centerline velocity decreases up to a point where the flow reversal is maximum, following which it increases. The variation of the mean-flow velocity along the wall-normal direction at two different streamwise locations are shown in Figs. 4(c) and 4(d) for $Re = 1850$ and 3350 , respectively. To perform a local stability analysis of these

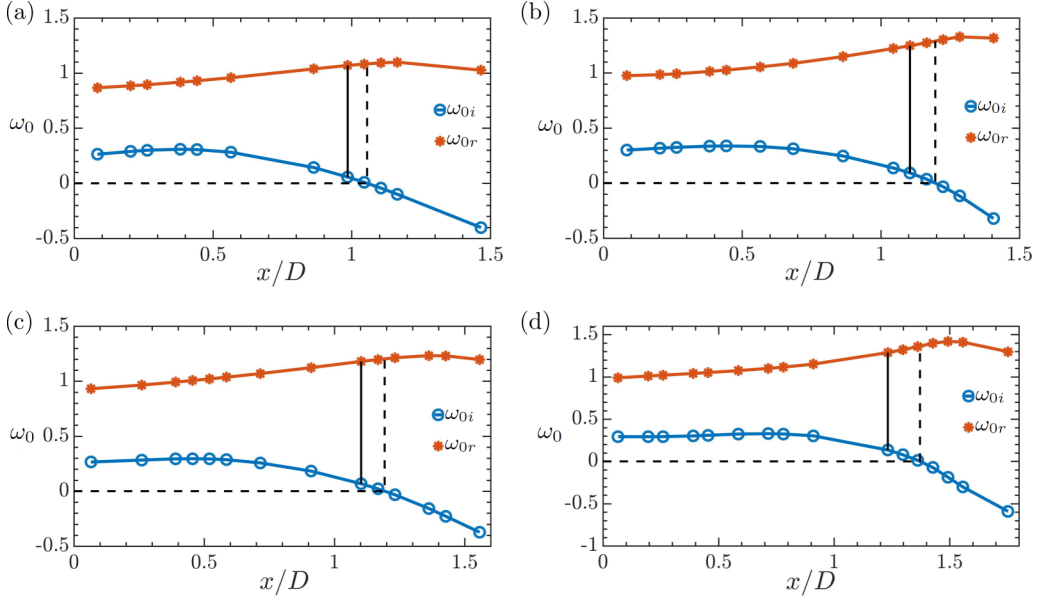


FIG. 6. Temporal amplification rate ω_{0i} (circles) and ω_{0r} (diamonds) as a function of the streamwise distance for the different flat plate wakes in the present study. The upper panels [(a) and (b)] correspond to the blunt trailing edge, while (c) and (d) for the circular trailing edge. The straight vertical line represents the stagnation point x_{st} , while the dashed line indicates the end of the AU region. Parameter settings: [(a) and (c)] $Re = 1850$ and [(b) and (d)] $Re = 3350$.

time-averaged velocity fields, as in other experimental [60,74] and numerical studies [46], it is convenient to fit the measured profiles using an analytical expression as

$$U(y) = c_1 \exp(-y^2/c_2) + c_3. \quad (17)$$

Here c_1 , c_2 , and c_3 are constants which were varied so as to best predict the measured experimental velocity profiles. Indeed, their values are different at each streamwise location. These are shown by the solid black lines in Figs. 4(c) and 4(d). The length of the recirculation zone, represented using the zero contour of the streamwise velocity field in Figs. 4(a) and 4(b), increases with the Reynolds number. This is elucidated in Fig. 5 where the variation of the centerline velocity downstream of the flat plate with a blunt trailing edge are shown in Figs. 5(a) and 5(b). The contours of the complex frequency ω in the complex k plane at the respective stagnation points for $Re = 1850$ and $Re = 3350$ are shown in Figs. 5(c) and 5(d).

To delineate the absolutely unstable (AU) region from the convectively unstable (CU), we extend the local analysis to the entire wake region. Figure 6 shows the variation of the real and imaginary parts of the absolute frequency ω_0 as a function of the downstream distance from the trailing edge of the flat plate. The AU region where $\omega_{0i} > 0$ is demarcated using dotted lines. It can be seen in Fig. 6 that the flow is locally AU both for blunt, and circular trailing edges directly downstream in the flat plate wake. The extent of the AU region indeed increases with the Reynolds number, beyond which the flows are CU. It is this boundary of the AU region which is of particular interest, as they are defined by real absolute frequencies [11,75]. It can be seen from Fig. 6 that the absolutely unstable region closely follows the flow reversal region, extending slightly beyond it. For $Re = 1850$ the distance between the stagnation point and the front of the AU region is $0.07D$, while for $Re = 3350$ is $0.09D$. This feature has also been observed in other bluff-body wake flows [11–13,17]. It can also be noted from Fig. 6 that the local frequency at a given streamwise location in the wake is higher at a larger Reynolds number.

TABLE I. Summary of the different characteristic frequencies (ω_{0r}) from the present study. Here ω_{st} and $\omega_{AU/CU}$ are the frequencies obtained from a local spatiotemporal analysis at the stagnation point and at the end of AU region, respectively. The experimentally measured shedding frequency is denoted by ω_{exp} . Here ω_{saddle} denotes the circular frequency obtained from the saddle-point criterion, and ω_{POD} obtained from the POD based low-dimensional model, as described below.

Trailing edge	Re	ω_{st}	$\omega_{AU/CU}$	ω_{exp}	ω_{saddle}	ω_{POD}
Blunt	1850	1.04	1.05	1.04	0.91	1.03
Blunt	3350	1.23	1.27	1.25	1.03	1.24
Circular	1850	1.16	1.18	1.19	1.0	1.22
Circular	3350	1.27	1.34	1.37	1.09	1.34

It has to be pointed out that unlike in cylinder wakes, the flow is AU at the trailing edge of the flat plate. In the former the flow goes from a locally CU domain to a finite sized region where the flow is locally AU. The frequency at this transition station, from local convective to absolute instability, fixes the global shedding frequency [12]. This arises from a balance between upstream perturbation growth from the AU region and downstream advection from the CU region resulting in a stationary front [12,40]. However, in flat plate wakes the flow is already AU at the trailing edge, and hence the global selection frequency outlined in Ref. [12] is not directly applicable to the present flows. We shall see that the other characteristic frequencies discussed in Ref. [12], notably the real absolute frequency corresponding to the AU/CU transition station [11], which corresponds to the criterion outlined in Ref. [37], and the local absolute frequency at the stagnation point, predicts the observed global shedding frequency. The nondimensional absolute frequency at any location can be calculated as

$$\omega_{0r} = 2\pi \left(\frac{fD}{U_\infty} \right). \quad (18)$$

For $Re = 1850$ the freestream velocity U_∞ is 2.42 m/s, whereas for $Re = 3350$, U_∞ is 4.38 m/s. The characteristic frequencies at some streamwise locations of interest, along with the experimentally measured values are presented in Table I. Figure 7 summarizes these experimentally measured

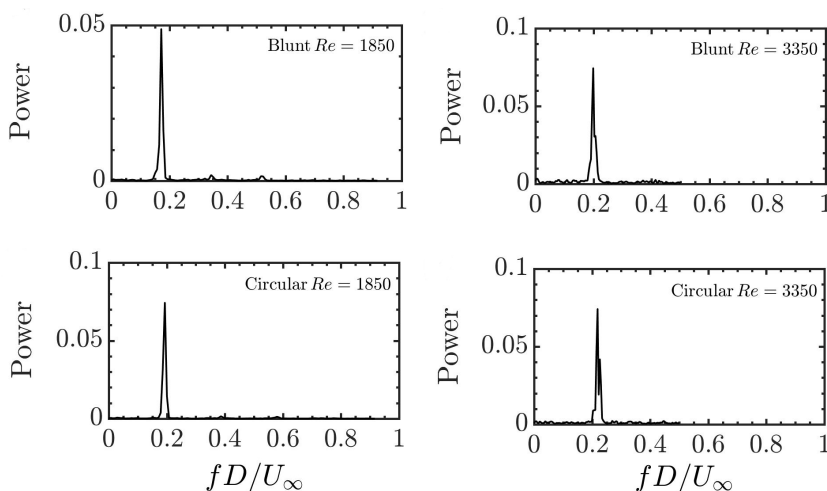


FIG. 7. The experimentally measured frequency spectra for the different cases considered in the present study. The global shedding frequency increases with the Reynolds number, and remains roughly the same irrespective of the trailing edge geometry.

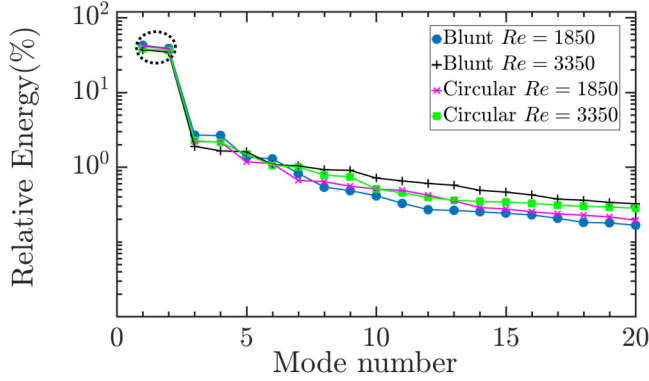


FIG. 8. The relative contribution of the POD modes to the total energy. It can be seen that the first two POD modes, which occur in pairs, contribute over 70% to the total energy in all the four different cases considered in the present study.

global shedding frequencies in the present study. They are in excellent agreement with the local absolute frequency at the streamwise location where the flow goes from an absolutely unstable to a convectively unstable region. It may be noted here that the circular frequency, ω_{saddle} , is obtained based on the analytical continuation of ω_0 in the complex x plane [13,65] following a second order polynomial fit through ω_0 as described in Ref. [76]. To further investigate this excellent agreement using the time-averaged velocity profiles, we perform the POD analysis of the fluctuating

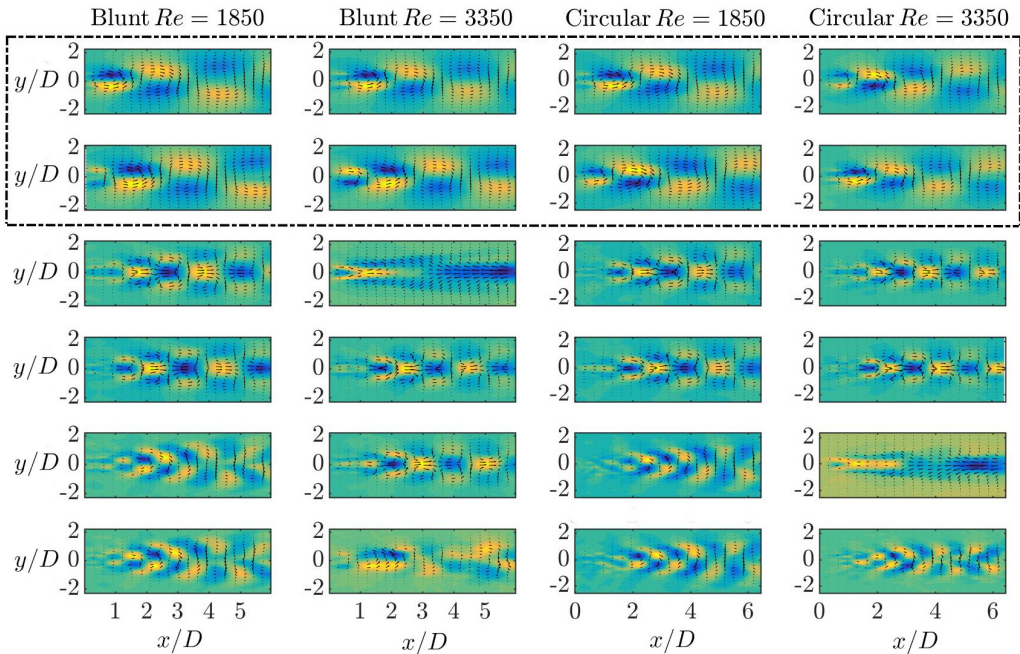


FIG. 9. The spatial distribution of the first six POD modes for the four different cases considered in the present study. The colormap indicates the streamwise component of the POD eigenfunction. It can be seen that the first two modes have the same spatial structure, albeit with a slight shift in the streamwise direction. The fact that the POD modes occur in pairs is also manifestly evident from their spatial distributions.

TABLE II. Relative and cumulative energy for the first 10 POD modes for four different cases.

Mode	Blunt	Blunt	Blunt	Blunt	Circular	Circular	Circular	Circular
	Re = 1850	Re = 1850	Re = 3350	Re = 3350	Re = 1850	Re = 1850	Re = 3350	Re = 3350
Number	Relative energy (%)	Cumulative energy (%)	Relative energy (%)	Cumulative energy (%)	Relative energy (%)	Cumulative energy (%)	Relative energy (%)	Cumulative energy (%)
1	42.60	42.60	37.10	37.10	41.50	41.50	38.08	38.08
2	38.68	81.30	34.42	71.52	38.00	79.50	36.13	74.20
3	2.68	83.98	1.89	73.41	2.20	81.70	2.25	76.45
4	2.63	86.61	1.65	75.05	2.16	83.86	2.14	78.60
5	1.35	87.96	1.60	76.66	1.18	85.03	1.48	80.08
6	1.29	89.25	1.07	77.74	1.10	86.14	1.05	81.13
7	0.82	90.08	1.04	78.77	0.66	86.80	1.00	82.14
8	0.54	90.62	0.92	79.69	0.64	87.44	0.78	82.92
9	0.48	91.10	0.90	80.56	0.55	87.99	0.74	83.66
10	0.41	91.52	0.71	81.31	0.51	88.50	0.51	84.17

velocity data; ω_{POD} in Table I is found from this analysis, which is presented in the following section.

IV. REDUCED ORDER MODELING

To quantify the interaction between the mean-flow harmonic and the higher harmonics, which is the crux of the theoretical criterion derived in Ref. [16], we look at the reduced order dimensionality of the flat plate wake. To begin with, we compute the energy contribution of the different POD modes. As outlined in the previous section, the eigenvalue corresponding to each POD mode represents the proportional contribution to the total energy content. Figure 8 describes the relative energy distribution of the modes, for the different cases investigated in the present study. The numerical values of the relative and the cumulative energy of the first 10 POD modes are also listed in Table II. One may notice that the first two POD modes are the dominant ones. To be specific, the first two modes carry about 81.3%, 71.5%, 79.5%, and 74.2% of the total energy, for Re = 1850 (blunt), Re = 3350 (blunt), Re = 1850 (circular), and Re = 3350 (circular) cases, respectively. Table II also shows that the first 10 POD modes carry more than 80% energy for all the cases. It also indicates that some eigenvalues come as pairs, for example, first two eigenvalues for all the cases; the corresponding modes are known as degenerate eigenmodes, which originate due to some symmetry in the flow [53,62,77,78], as further discussed below. Similar observations have also been made in the case of cylinder wakes [51,54,79].

The POD modes or the eigenfunctions corresponding to the first six eigenvalues are shown in Fig. 9. The corresponding time coefficients obtained from direct projections [Eq. 10] and their frequency spectra are shown in Figs. 10 and 11, respectively. The first two near-degenerate POD modes are nearly the same with a slight spatial and temporal shift as seen in Figs. 9 and 10, respectively. This sort of shift associated with a pair of POD modes is attributed to some sort of symmetry/traveling disturbance in the flow. Here, this is due to the vortex shedding at the trailing edge of the flat plate, as the frequency of these disturbances in Fig. 11 (first row) matches with the shedding frequency in Fig. 7. Similarly, second and third pairs of modes corresponding to the second and third pairs of eigenvalues, for Re = 1850 (blunt) and Re = 1850 (circular) cases, show the first and the second harmonics associated with the vortex shedding. In contrast, one solitary mode which does not make any pair is seen to appear for the blunt and circular cases at Re = 3350, mode 3 and mode 5, respectively. This mode is similar to the anomalous mode of first kind reported by Sengupta *et al.* [79] where they investigated the instability of a flow past a circular cylinder. They

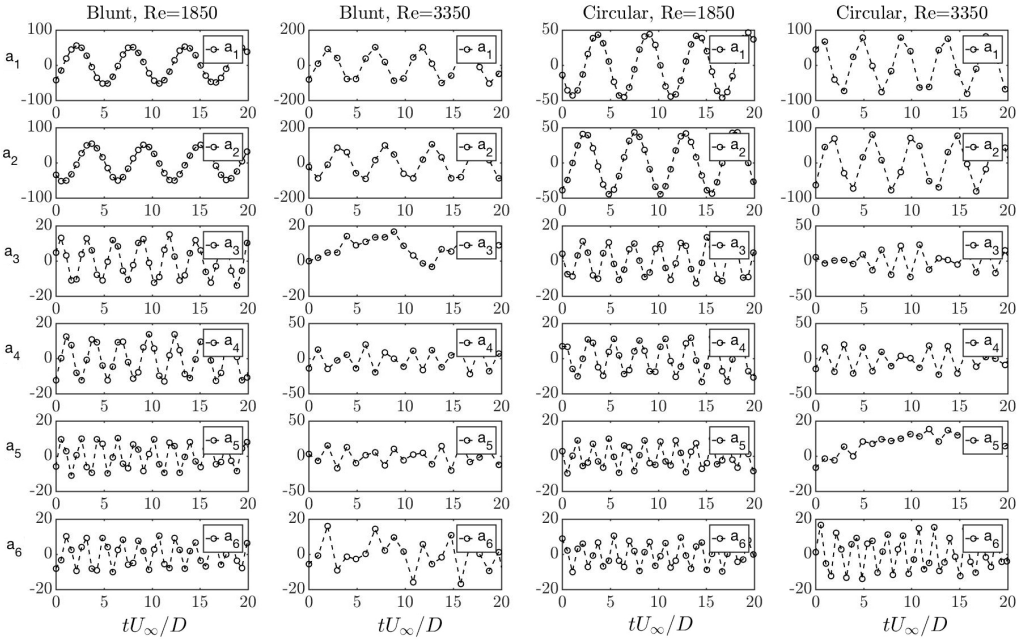


FIG. 10. The projected POD coefficients, a^k , corresponding to the POD modes shown in Fig. 9.

attributed the appearance of this mode due to transient effects in the flow. This phenomenon has also been investigated by Noack *et al.* [51] where they constructed a shift mode using the steady solution and the time-averaged solution for a better resolution of the transient dynamics.

The spatial structure of this anomalous mode is shown in Fig. 9 (second column 3rd mode, and fourth column fifth mode). The corresponding time series and frequency of this mode is shown in Figs. 10 and 11, for the blunt and the circular cases at $Re = 3350$. These observations indicate that this mode may be associated with a slowly moving disturbance in the downstream direction. Interestingly, these results also show that the trailing edge geometry has little influence on the vortex shedding characteristics, whereas the Reynolds number does play a significant role. Further, the present POD analysis reveals that the flat plate wake at this moderate Reynolds number is low dimensional in nature as the first ten POD modes can capture more than 80% of the flow energy. Since the first two POD modes contribute maximum to the total energy as shown in Fig. 8, it is worthwhile to compare these modes with the linear stability analysis. This is shown in Fig. 12 where the streamwise and cross-stream components of the eigenfunctions obtained from the linear stability analysis is compared with those obtained from POD analysis and experimental data. The peak of the streamwise component shown in Fig. 12(a) is slightly away from the experimental data point. This may be attributed to the fact that the linear stability analysis was performed using the velocity profiles which were curve-fitted to the experimental data as discussed earlier. The mismatch of the POD eigenmode with that obtained from the linear stability analysis and experimental data, at the outer side ($y/D \approx 1$) of the shear layer, is due to the fact that we have considered the absolute value of the POD mode. However, the cross-stream component shows an excellent agreement with the experimental data as well as with the POD eigenfunction.

Since the vortex shedding dynamics is low dimensional, it is interesting to check whether a reduced order model/low-dimensional model can describe the vortex shedding characteristics. Considering just two POD modes, Eq. (13) was numerically solved in Matlab. Figure 13 shows the numerical solutions for a_1 and a_2 compared with their experimental counter parts obtained using direct projection for all the cases considered in the present study. It can be seen that the coefficients

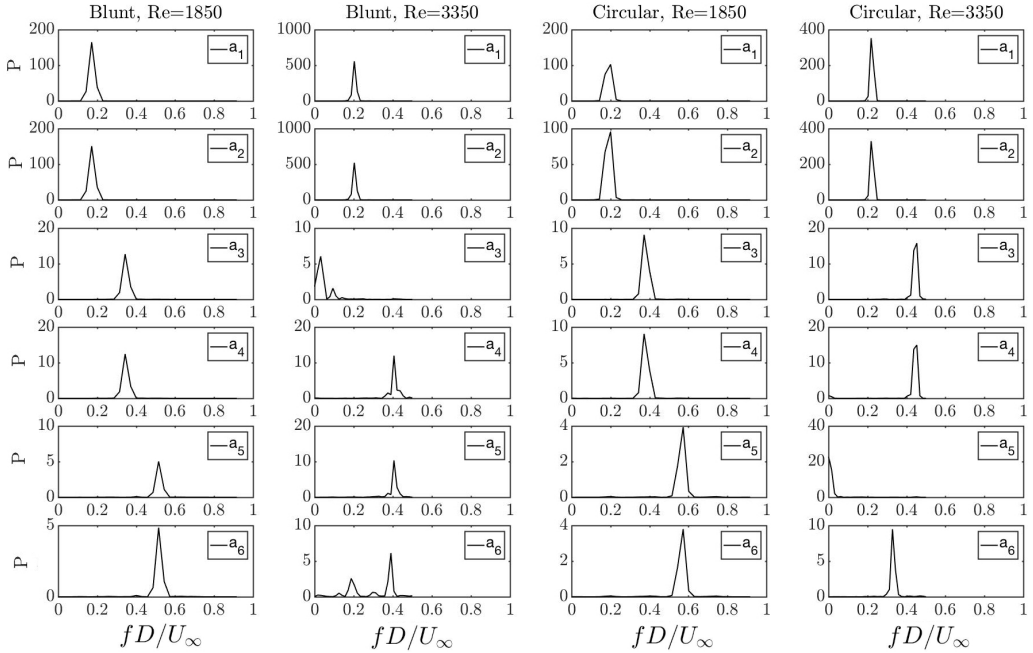


FIG. 11. Spectra of the POD coefficients, a^k , shown in Fig. 10. P indicates power in arbitrary scales.

of the first two modes closely follow the experimental data. The simulated frequencies associated with the first two POD modes, and the experimentally measured global shedding frequency from the instantaneous velocity fields are shown in Fig. 14. One may notice an excellent agreement between the numerical solution and the experimental data, at least for one shedding cycle. However, a phase drift can be observed in Fig. 13 during the time evolution of the coefficients. This phenomenon has been reported in various studies in the past [80–84]. It arises mainly due to numerical differentiation of the higher-order modes which have a lower energy content but with higher noise levels. This can be seen in Fig. 13 where the phase drift is higher for the six-mode model. In fact inclusion of more number of modes while solving Eq. (13) does not improve the solution significantly. Although the amplitudes are found to be comparable with the experimental data for the four and six mode models, there is a significant deviation of phase as the solution progresses in time, which is better seen for the higher Re cases considered here.

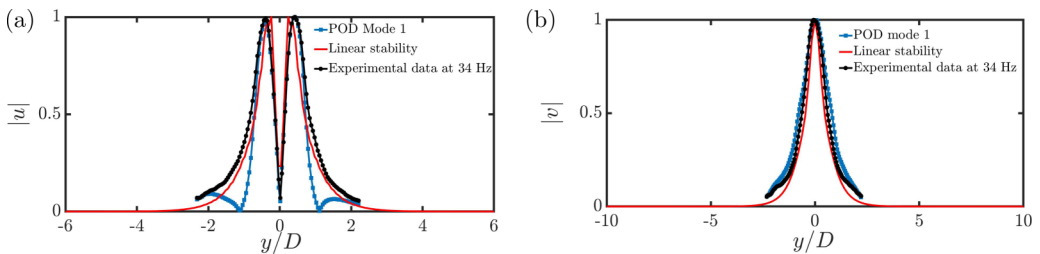


FIG. 12. Absolute values of the streamwise ($|u| = |u_x|/|u_x|_{\max}$) and cross-stream ($|v| = |u_y|/|u_y|_{\max}$) components of the eigenfunctions computed from linear stability analysis, POD analysis and experimental data for the flat plate with a blunt trailing edge. Parameter settings: $Re = 1850$, blunt trailing edge. The comparison is shown at the streamwise location corresponding to the end of the AU region ($x/D = 1.04$). Experimental data at 34Hz is considered as it is the vortex shedding frequency ($\omega_{\text{exp}} = 1.04$, as shown in Table I).

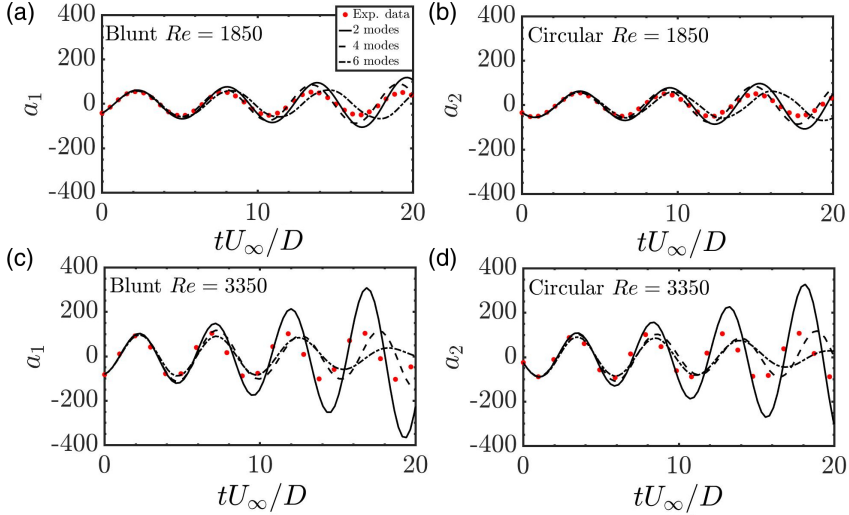


FIG. 13. Comparison of the simulated coefficients (solid line), a_1 and a_2 , obtained using different number of modes in the reduced order model (two, four, and six modes), with their experimental counter parts (red filled circles), calculated from direct projection, for the different cases considered in the present study.

Nonetheless, the POD based simulations and the local stability analyses considering the time-averaged mean flow as the base flow gives an accurate estimation of the global shedding frequency of the wake, as shown in Fig. 14. We now turn our attention to provide a plausible explanation based on the theoretical criterion outlined by Sipp and Lebedev [16]. For doing this we compare the interaction strength between the mean flow and the first harmonic, and the interaction strength of the second harmonic with the first. From our framework based on low-dimensional modeling

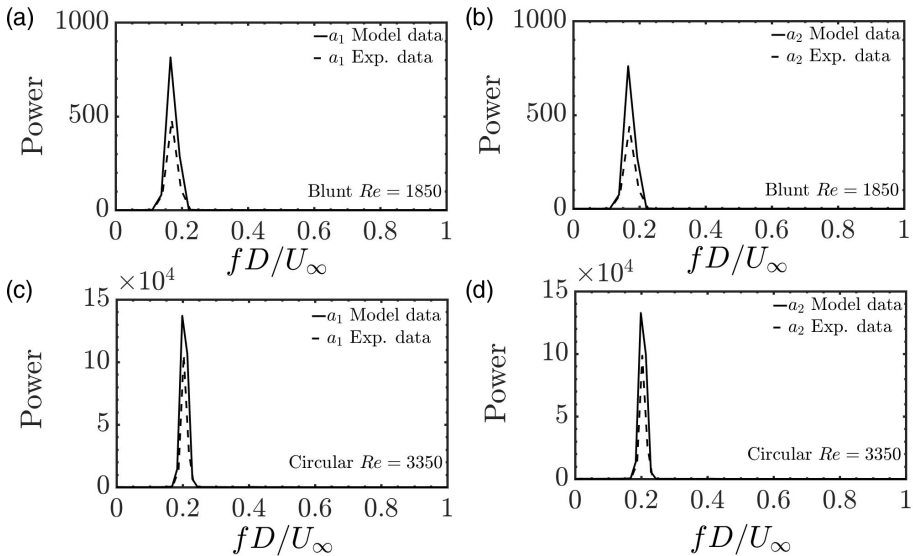


FIG. 14. Comparison of the frequency spectra of the time coefficients, a_1 and a_2 obtained from the simulation (solid line), and from the direct projection (dashed line). They are in excellent agreement in all the four different cases investigated.

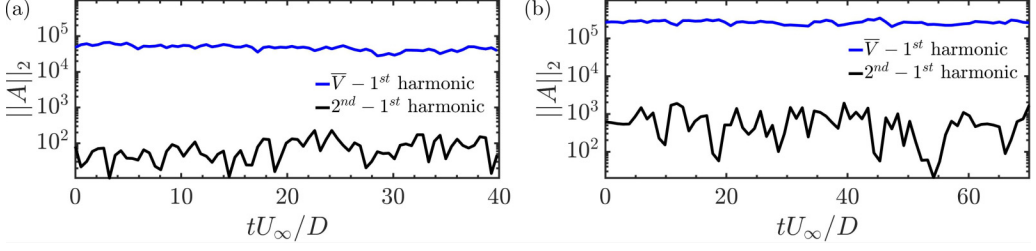


FIG. 15. Representative measure of the interaction strengths between the mean-flow and the higher harmonics. The interaction strength between the mean-flow and first harmonic is shown using a blue line while the black line shows the interaction strength between the second and the first harmonic. Parameter settings: (a) blunt trailing edge, $\text{Re} = 1850$; (b) circular trailing edge, $\text{Re} = 3350$.

[Eq. (14)], we introduce the following ansatz as a representative measure of the interaction strength between the mean flow ($\bar{\mathbf{V}}$) and the first harmonic (given by Φ^1 and Φ^2):

$$A^{11} = -(\Phi^1, \Phi^1 \cdot \nabla \bar{\mathbf{V}}) - (\Phi^1, \bar{\mathbf{V}} \cdot \nabla \Phi^1), \quad (19)$$

$$A^{12} = -(\Phi^1, \Phi^2 \cdot \nabla \bar{\mathbf{V}}) - (\Phi^1, \bar{\mathbf{V}} \cdot \nabla \Phi^2), \quad (20)$$

$$A^{21} = -(\Phi^2, \Phi^1 \cdot \nabla \bar{\mathbf{V}}) - (\Phi^2, \bar{\mathbf{V}} \cdot \nabla \Phi^1), \quad (21)$$

$$A^{22} = -(\Phi^2, \Phi^2 \cdot \nabla \bar{\mathbf{V}}) - (\Phi^2, \bar{\mathbf{V}} \cdot \nabla \Phi^2), \quad (22)$$

$$A = \begin{bmatrix} A^{11} & A^{12} \\ A^{21} & A^{22} \end{bmatrix}. \quad (23)$$

Note that while evaluating the matrix A the modes are weighted by their corresponding amplitudes obtained from the direct projection, and the viscous terms have been neglected. To measure the interaction strength of the second harmonic with the first harmonic using the same mathematical ansatz, we replace (Φ^1, Φ^2) with (Φ^3, Φ^4) and $\bar{\mathbf{V}}$ with $(a_1 \Phi^1 + a_2 \Phi^2)$ in the above set of equations. We would like to remind the reader that the norm of the above formed matrix A is only a representative measure of the interaction strengths and is considered as it follows directly from the framework of reduced-order modeling. Figure 15 shows the evolution of these quantities of interest over multiple shedding cycles. We can see from Figs. 15(a) and 15(b) that the interaction strength between the mean-flow and the first harmonic is several orders of magnitude higher than the interaction strength between the second and the first harmonics. We have also observed that the interaction strength between the mean flow and the second harmonic is about ten times smaller when compared with that of the first harmonic, which is not shown here.

These findings reaffirm the fact that there is a strong interaction of the mean flow (zeroth harmonic) with the first harmonic in comparison with the higher harmonics. To further verify the interaction strengths between the mean-flow and higher harmonics we have computed the contributions of different terms present in Eq. (13). These are summarized in Fig. 16. One can clearly see that while keeping only the contribution from the A term [Eq. (14)] the flow unsteadiness is accurately captured over several shedding cycles. The importance of the contribution stemming from A [Eq. (14)] can be seen from the blue curves which fails to capture the experimental data even qualitatively. Interestingly by just turning-off the diagonal terms of A in Eq. (13) one can reproduce the flow dynamics quantitatively (pink curves). This aspect has not been previously reported in the literature to the best of our knowledge. Similarly, when one switches-off the B term in Eq. (13), an accurate estimate of the frequency can be obtained albeit with a difference in the amplitude. It can also be noted from Fig. 16(b) that the four-mode model does not improve significantly the captured dynamics. However, a small phase drift can be noticed during the time evolution for the case corresponding to the four-mode model when the B term is turned off. One has to keep in mind that the two-mode model considers the interaction of the mean flow with the first harmonic, whereas

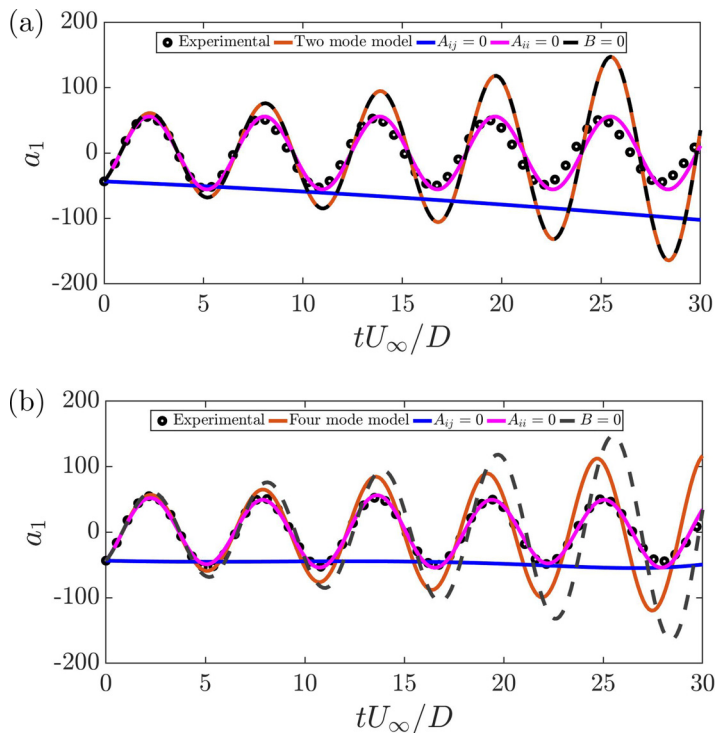


FIG. 16. Comparison of the experimental data with the simulations by considering the contribution of the different terms in Eq. (13). (a) Two-mode model and (b) four-mode model. Parameter settings: $Re = 1850$, blunt trailing edge.

the four-mode model takes into account of both the first and second harmonic interacting with the mean flow. These observations clearly signify that the interaction strength between the zeroth (mean flow) and the first harmonic is the dominant one. This is consistent with the theoretical finding presented in Ref. [16], and in turn explains why the mean-flow velocity fields gives an accurate estimate of the global unsteadiness, thereby experimentally supporting the criterion outlined by Sipp and Lebedev [16].

V. DISCUSSION AND CONCLUDING REMARKS

The global shedding frequency of the flat plate wake is well predicted from a local spatiotemporal stability analysis based on the mean-flow velocity fields. The mean-flow velocity fields were obtained using a TR-PIV technique in a low-speed wind tunnel. Two values of the Reynolds number, Re , based on the freestream velocity U_∞ and the flat plate thickness D (which is fixed throughout the study), were considered: 1850 and 3350. A blunt, and a circular profile is used for the trailing edge geometry of the flat plate. Though the time-mean velocity profiles at different streamwise locations can be obtained using the hotwire anemometry technique (as in Ref. [41]), the present investigation uses a nonintrusive PIV measurement technique. This measurement technique is best suited for separating flows like the present one, and it is widely used for simultaneous whole field measurements as compared to the hotwire anemometry technique. The local stability analysis assumes that the flows are nearly parallel in the regions where the stability analysis is performed. Despite this, as observed in earlier studies, notably the vortex shedding from interacting boundary layers at a blunt trailing edge of a rectangular forebody in Ref. [13] which was studied numerically, the selected frequency is surprisingly well estimated with a deviation within 1%. In addition, the

frequency at the end of the absolutely unstable region is seen to be selected by the global wake in the present study, which is the hydrodynamic resonance criterion advanced by Koch [37]. Similar observations have been detailed for a cylinder wake based on the mean flow [12,41].

As discussed in Ref. [12], the linear global frequency corresponding to the streamwise locations where the flow changes the nature of instability from convective to absolute cannot account for the real global frequency selected by the wake. In addition, the saddle-point criterion gave the best estimate for the shedding frequency of the fully developed cylinder wake when the stability analysis was applied on the time-averaged mean flow. This has been theoretically [16], numerically [14,15], and experimentally [41] supported. The same characteristics have been observed in the present study based on time-averaged mean-flow fields for a flat plate wake, with the frequencies obtained from a local stability analysis providing excellent predictions for the global shedding frequency. Interestingly, as observed in other wake flow studies, the local absolute frequency at the stagnation point was found to give an excellent estimate of the global shedding frequency. We would like to emphasize that to the best of our knowledge, this is the first experimental study to quantitatively investigate the global shedding frequency of a flat plate wake, and compare the different selection criteria available in literature using mean-flow velocity fields.

To further support these observations, we have performed a POD analysis using the velocity fluctuations. It has been shown that the first two POD modes (which occur in pairs) account for over 70% of the total energy of the flow. The frequency of the wake predicted using a low-dimensional model with these two modes are in excellent agreement with the experimentally measured values. The physical mechanism behind the two theoretical conditions presented in Ref. [16] is related to the fact that the frequency of the nonlinearly saturated limit cycle of the unsteady wake depends on the interaction of the mean flow with the higher harmonics. We have observed that the interaction strength of the mean-flow and first harmonic is significantly higher than the interaction strength between the second and the first harmonics. This quantitatively supports the theoretical criterion outlined by Sipp and Lebedev [16] for the first time using experimentally measured flow fields. The reduced order framework considered here allows one to estimate the interaction strengths between the mean-flow and higher harmonics which can be used in other bluff-body flows as well. More importantly, Eq. (13), which closely mimics the flow dynamics without considering the B term and the diagonal terms in A , gives a linear framework, which is highly desirable in flow control applications.

ACKNOWLEDGMENTS

D.D., I.K., and A.C.M. acknowledge the financial support provided by IIT Kanpur for the TR-PIV system. Dr. G Balamurugan and Mr. Esvar Sunder are also acknowledged for their assistance with the data analyses and the TR-PIV measurements. We thank Mr. Abhinath Kr. Yadav and Mr. Dorilal for their help with the experimental setup in the wind tunnel. We also thank Mr. Aniffa and Mr. Vivek Kumar for their assistance with the error analysis. We would like to thank the referees who suggested numerous ways to improve the article. We would also like to thank Prof. Sudib Kumar Mishra for fruitful discussions regarding the manuscript.

-
- [1] V. Strouhal, Uber eube besondere art der tonerregung, *Annalen der Physik*. **241**, 216 (1878).
 - [2] A. Roshko, On the wake and drag of bluff bodies, *J. Aeronaut. Sci.* **22**, 124 (1955).
 - [3] A. B. Bauer, Vortex shedding from thin flat plates parallel to the free stream, *J. Aerosp. Sci.* **28**, 340 (1961).
 - [4] S. Bloor, The transition to turbulence in the wake of a circular cylinder, *J. Fluid Mech.* **19**, 290 (1964).
 - [5] P. Huerre and L. Redekopp, Local and global instabilities in spatially developing flows, *Annu. Rev. Fluid Mech.* **22**, 473 (1990).
 - [6] C. H. K. Williamson, Vortex dynamics in the cylinder wake, *Annu. Rev. Fluid Mech.* **28**, 477 (1996).

- [7] J.-M. Chomaz, P. Huerre, and L. Redekopp, A frequency selection criterion in spatially developing flows, *Stud. Appl. Maths* **84**, 119 (1991).
- [8] C. H. K. Williamson, Detuning a universal and continuous Strouhal–Reynolds number relationship for the laminar vortex shedding of a circular cylinder, *Phys. Fluids* **31**, 2742 (1988).
- [9] P. Monkewitz, The absolute and convective nature of instability in two-dimensional wakes at low Reynolds numbers, *Phys. Fluids* **31**, 999 (1988).
- [10] P. Monkewitz, P. Huerre, and J.-M. Chomaz, Global linear stability analysis of weakly non-parallel shear flows, *J. Fluid Mech.* **251**, 1 (1993).
- [11] B. Pier and P. Huerre, Nonlinear self-sustained structures and fronts in spatially developing wake flows, *J. Fluid Mech.* **435**, 145 (2001).
- [12] B. Pier, On the frequency selection of finite-amplitude vortex shedding in the cylinder wake, *J. Fluid Mech.* **458**, 407 (2002).
- [13] D. Hammond and L. Redekopp, Global dynamics of symmetric and asymmetric wakes, *J. Fluid Mech.* **231**, 231 (1997).
- [14] D. Barkley, Linear analysis of the cylinder wake mean flow, *Europhys. Lett.* **75**, 750 (2006).
- [15] S. Mittal, Global linear stability analysis of time-averaged flows, *Int. J. Numer. Methods Fluids* **58**, 111 (2008).
- [16] D. Sipp and A. Lebedev, Global stability of base and mean flows: a general approach and its applications to cylinder and open cavity flows, *J. Fluid Mech.* **593**, 333 (2007).
- [17] Y. Hwang and H. Choi, Control of absolute instability by basic-flow modification in a parallel wake at low Reynolds number, *J. Fluid Mech.* **560**, 465 (2006).
- [18] F. Gianetti and P. Luchini, Structural sensitivity of the first instability of the cylinder wake, *J. Fluid Mech.* **581**, 167 (2007).
- [19] H. Sato and K. Kuriki, The mechanism of transition in the wake of a thin flat plate placed parallel to a uniform flow, *J. Fluid Mech.* **11**, 321 (1961).
- [20] D. R.-S. Ko, T. Kubota, and L. Lees, Finite disturbance effect on the stability of a laminar incompressible wake behind a flat plate, *J. Fluid Mech.* **40**, 315 (1970).
- [21] M. Nishioka and T. Miyagi, Measurements of velocity distributions in the laminar wake of a flat plate, *J. Fluid Mech.* **84**, 705 (1978).
- [22] B. R. Ramaprian, V. C. Patel, and M. S. Sastry, The symmetric turbulent wake of a flat plate, *AIAA J.* **20**, 1228 (1982).
- [23] I. Wygnanski, F. Champagne, and B. Marasli, On the large-scale structures in two-dimensional, small-deficit, turbulent wakes, *J. Fluid Mech.* **168**, 31 (1986).
- [24] S. Jovic and B. R. Ramaprian, *Large-scale Structure of the Turbulent Wake behind a Flat Plate*, Technical Report, IIHR Report No. 298, Iowa Institute of Hydraulic Research, The University of Iowa (1986).
- [25] E. A. Bogucz and J. D. A. Walker, The turbulent near wake at a sharp trailing edge, *J. Fluid Mech.* **196**, 555 (1988).
- [26] S. Julien, J. Lasheras, and J.-M. Chomaz, Three-dimensional instability and vorticity patterns in the wake of a flat plate, *J. Fluid Mech.* **479**, 155 (2003).
- [27] J. C. Lasheras and E. Meiburg, Three-dimensional vorticity modes in the wake of a flat plate, *Phys. Fluids* **2**, 371 (1990).
- [28] R. Narasimha and A. Prabhu, Equilibrium and relaxation in turbulent wakes, *J. Fluid Mech.* **54**, 1 (1972).
- [29] M. Carini, C. Airiau, A. Debien, O. Léon, and J. O. Pralits, Global stability and control of the confined turbulent flow past a thick flat plate, *Phys. Fluids* **29**, 024102 (2017).
- [30] C. H. Sieverding and H. Heinemann, The influence of boundary layer state on vortex shedding from flat plates and turbine cascades, *J. Turbomach.* **112**, 181 (1990).
- [31] Y. Nakamura, Y. Ohya, and H. Tsuruta, Experiments on vortex shedding from flat plates with square leading and trailing edges, *J. Fluid Mech.* **222**, 437 (1991).
- [32] M. M. Rai, *Flat Plate Wake Velocity Statistics Obtained with Circular and Elliptic Trailing Edges*, Technical Report, NASA/TM-2016-219154 (2016).
- [33] Z. J. Taylor, E. Palombi, R. Gurka, and G. A. Kopp, Features of the turbulent flow around symmetric elongated bluff bodies, *J. Fluids Struct.* **27**, 250 (2011).

- [34] D. R. Boldman, P. F. Brinich, and M. E. Goldstein, Vortex shedding from a blunt trailing edge with equal and unequal external mean velocities, *J. Fluid Mech.* **75**, 721 (1976).
- [35] A. Rowe, A. L. A. Fry, and F. Motallebi, Influence of boundary-layer thickness on base pressure and vortex shedding frequency, *AIAA J.* **39**, 754 (2001).
- [36] V. Durgesh, J. W. Naughton, and S. A. Whitmore, Experimental investigation of base-drag reduction via boundary-layer modification, *AIAA J.* **51**, 416 (2013).
- [37] W. Koch, Local instability characteristics and frequency determination of self-excited wake flows, *J. Sound Vib.* **99**, 53 (1985).
- [38] R. T. Pierrehumbert, Local and global baroclinic instability of zonally varying flow, *J. Atmos. Sci.* **41**, 2141 (1984).
- [39] P. A. Monkewitz and L. N. Nguyen, Absolute instability in the near-wake of two-dimensional bluff bodies, *J. Fluids Struct.* **1**, 165 (1987).
- [40] G. Dee and J. S. Langer, Propagating pattern selection, *Phys. Rev. Lett.* **50**, 383 (1983).
- [41] M. Khor, J. Sheridan, M. C. Thompson, and K. Hourigan, Global frequency selection in the observed time-mean wakes of circular cylinders, *J. Fluid Mech.* **601**, 425 (2008).
- [42] K. Ryan, M. C. Thompson, and K. Hourigan, Three-dimensional transition in the wake of bluff elongated cylinders, *J. Fluid Mech.* **538**, 1 (2005).
- [43] A. Naghib-Lahouti, L. S. Doddipatla, and H. Hangan, Secondary wake instabilities of a blunt trailing edge profiled body as a basis for flow control, *Exp. Fluids* **52**, 1547 (2012).
- [44] A. Naghib-Lahouti, P. Lavoie, and H. Hangan, Wake instabilities of a blunt trailing edge profiled body at intermediate reynolds numbers, *Exp. Fluids* **55**, 1779 (2014).
- [45] L. S. Doddipatla, Wake dynamics and passive flow control of a blunt trailing edge profiled body, Ph.D. thesis, The University of Western Ontario, 2010.
- [46] S. Julien, S. Ortiz, and J. M. Chomaz, Secondary instability mechanisms in the wake of a flat plate, *Eur. J. Mech. B Fluids* **23**, 157 (2004).
- [47] T. Leweke and C. H. K. Williamson, Three-dimensional instabilities in wake transition, *Eur. J. Mech. B Fluids* **17**, 571 (1998).
- [48] D. Barkley and R. D. Henderson, Three-dimensional Floquet stability analysis of the wake of a circular cylinder, *J. Fluid Mech.* **322**, 215 (1996).
- [49] P. Huerre and P. A. Monkewitz, Open shear flow instabilities, in *Perspectives in Fluid Dynamics: A Collective Introduction to Current Research*, edited by G. K. Batchelor, H. K. Moffatt, and M. G. Worster (Cambridge University Press, Cambridge, UK, 2000).
- [50] N. Aubry, P. Holmes, J. L. Lumley, and E. Stone, The dynamics of coherent structures in the wall region of a turbulent boundary layer, *J. Fluid Mech.* **192**, 115 (1988).
- [51] B. R. Noack, K. Afanasiev, M. Morzynski, G. Tadmor, and F. Thiele, A hierarchy of low-dimensional models for the transient and post-transient cylinder wake, *J. Fluid Mech.* **497**, 335 (2003).
- [52] G. Berkooz, P. Holmes, and J. L. Lumley, The proper orthogonal decomposition in the analysis of turbulent flows, *Annu. Rev. Fluid Mech.* **25**, 539 (1993).
- [53] D. Rempfer and H. F. Fasel, Evolution of three-dimensional coherent structures in a flat-plate boundary layer, *J. Fluid Mech.* **260**, 351 (1994).
- [54] S. G. Siegel, J. Seidel, C. Fagley, D. M. Luchtenburg, K. Cohen, and T. McLaughlin, Low-dimensional modelling of a transient cylinder wake using double proper orthogonal decomposition, *J. Fluid Mech.* **610**, 1 (2008).
- [55] B. Galletti, C. H. Bruneau, L. Zannetti, and A. Iollo, Low-order modelling of laminar flow regimes past a confined square cylinder, *J. Fluid Mech.* **503**, 161 (2004).
- [56] D. M. Luchtenburg, B. R. Noack, and M. Schlegel, An introduction to the POD Galerkin method for fluid flows with analytical examples and MATLAB source codes, Berlin Inst. Tech. MB1, Muller-Breslau-Strabe **11** (2009).
- [57] I. Kanshana, E. Sunder, and A. C. Mandal, Low dimensional modeling of flow behind a flat plate with blunt trailing edge, in *Proceedings of the 7th International and 45th National Conference on Fluid Mechanics and Fluid Power (FMFP'18)* (Indian Institute of Technology, Bombay, Mumbai, 2018).

- [58] D. Rempfer and H. Fasel, The dynamics of coherent structures in a flat-plate boundary layer, *Appl. Sci. Res.* **51**, 73 (1993).
- [59] M. Rajaei, S. K. F. Karlsson, and L. Sirovich, Low-dimensional description of free-shear-flow coherent structures and their dynamical behaviour, *J. Fluid Mech.* **258**, 1 (1994).
- [60] G. Balamurugan and A. C. Mandal, Experiments on localized secondary instability in bypass boundary layer transition, *J. Fluid Mech.* **817**, 217 (2017).
- [61] L. Lourenco, TRUE resolution PIV: a mesh-free second order accurate algorithm, *10th Int. Symp. on Applications of Laser Techniques in Fluid Mechanics (Lisbon)*, (2000).
- [62] A. C. Mandal, L. Venkatakrishnan, and J. Dey, A study on boundary-layer transition induced by free-stream turbulence, *J. Fluid Mech.* **660**, 114 (2010).
- [63] A. C. Mandal and J. Dey, An experimental study of boundary layer transition induced by a cylinder wake, *J. Fluid Mech.* **684**, 60 (2011).
- [64] P. Phani Kumar, A. C. Mandal, and J. Dey, Effect of a mesh on boundary layer transitions induced by free-stream turbulence and an isolated roughness element, *J. Fluid Mech.* **772**, 445 (2015).
- [65] J.-M. Chomaz, Global instabilities in spatially developing flows: Non-normality and nonlinearity, *Annu. Rev. Fluid Mech.* **37**, 357 (2005).
- [66] P. Darzin and W. Reid, *Hydrodynamic Stability* (Cambridge University Press, Cambridge, UK, 1981).
- [67] F. M. White and I. Corfield, *Viscous Fluid Flow*, Vol. 3 (McGraw-Hill New York, 2006).
- [68] L. N. Trefethen, *Spectral Methods in MATLAB* (SIAM, Philadelphia, PA, 2000).
- [69] A. Bers, *Space-time evolution of plasma instabilities—absolute and convective*, in Handbook of Plasma Physics, 1961.
- [70] R. Briggs, *Election-Stream Interaction with Plasmas* (MIT Press, Cambridge, UK, 1964).
- [71] L. Sirovich, Turbulence and the dynamics of coherent structures. part i: Coherent structures, *Q. Appl. Math.* **45**, 561 (1987).
- [72] J. Pedersen and K. Meyer, Pod analysis of flow structures in a scale model of a ventilated room, *Exp. Fluids* **33**, 940 (2002).
- [73] D. Rempfer, Investigations of boundary layer transition via Galerkin projections on empirical eigenfunctions, *Phys. Fluids* **8**, 175 (1996).
- [74] M. Asai, M. Minagawa, and M. Nishioka, The instability and breakdown of a near-wall low-speed streak, *J. Fluid Mech.* **455**, 289 (2002).
- [75] B. Pier, P. Huerre, J.-M. Chomaz, and A. Couairon, Steep nonlinear global modes in spatially developing media, *Phys. Fluids* **10**, 2433 (1998).
- [76] S. J. Rees, Hydrodynamic instability of confined jets and wakes and implications for gas turbine fuel injectors, Ph.D. thesis, University of Cambridge, 2009.
- [77] A. E. Deane, I. G. Kevrekidis, G. E. Karniadakis, and S. A. Orszag, Low-dimensional models for complex geometry flows: Application to grooved channels and circular cylinders, *Phys. Fluids* **3**, 2337 (1991).
- [78] N. Aubry, R. Guyonnet, and R. Lima, Spatio-temporal symmetries and bifurcations via bi-orthogonal decompositions, *J. Nonlin. Sci.* **2**, 183 (1992).
- [79] T. K. Sengupta, N. Singh, and V. K. Suman, Dynamical system approach to instability of flow past a circular cylinder, *J. Fluid Mech.* **656**, 82 (2010).
- [80] C. W. Rowley, *Modeling, Simulation, and Control of Cavity Flow Oscillations*, PhD thesis, California Institute of Technology (2002).
- [81] X. Ma, G. E. Karniadakis, H. Park, and M. Gharib, DPIV-driven flow simulation: A new computational paradigm, *Proc. Roy. Soc. Lond. Ser. A: Math. Phys. Eng. Sci.* **459**, 547 (2003).
- [82] D. Moreno, A. Krothapalli, M. B. Alkisar, and L. M. Lourenco, Low-dimensional model of a supersonic rectangular jet, *Phys. Rev. E* **69**, 026304 (2004).
- [83] B. R. Noack, P. Papas, and P. A. Monkewitz, The need for a pressure-term representation in empirical Galerkin models of incompressible shear flows, *J. Fluid Mech.* **523**, 339 (2005).
- [84] N. Hasan and S. Sanghi, Proper orthogonal decomposition and low-dimensional modelling of thermally driven two-dimensional flow in a horizontal rotating cylinder, *J. Fluid Mech.* **573**, 265 (2007).